RESEARCH ARTICLE

Chemical in-depth analysis of (Ca/Sr)F$_2$ core–shell like nanoparticles by X-ray photoelectron spectroscopy with tunable excitation energy

Anja Müller[1,2] ⓘ | Thoralf Krahl[1] | Jörg Radnik[2] ⓘ | Andreas Wagner[2] | Carsten Kreyenschulte[3] | Wolfgang S.M. Werner[4] | Benjamin Ritter[1] | Erhard Kemnitz[1] | Wolfgang E.S. Unger[1,2] ⓘ

[1]Department of Chemistry, Humboldt-Universität zu Berlin, Berlin, Germany

[2]Surface Analysis and Interfacial Chemistry, Bundesanstalt für Materialforschung und -prüfung (BAM), Berlin, Germany

[3]Electron Microscopy, Leibniz-Institut für Katalyse e.V. (LIKAT), Rostock, Germany

[4]Applied and Computational Physics, Technische Universität Wien, Vienna, Austria

Correspondence
Erhard Kemnitz and Wolfgang E. S. Unger, Humboldt-Universität zu Berlin, Brook-Taylor-Straße 2, Berlin 12489, Germany.
Email: erhard.kemnitz@chemie.hu-berlin.de; wolfgang.unger@alumni.hu-berlin.de

Funding information
European Metrology Programme for Innovation and Research (EMPIR), Grant/Award Number: InNanoPart 14IND12

The fluorolytic sol–gel synthesis is applied with the intention to obtain two different types of core–shell nanoparticles, namely, SrF$_2$–CaF$_2$ and CaF$_2$–SrF$_2$. In two separate fluorination steps for core and shell formation, the corresponding metal lactates are reacted with anhydrous HF in ethylene glycol. Scanning transmission electron microscopy (STEM) and dynamic light scattering (DLS) confirm the formation of particles with mean dimensions between 6.4 and 11.5 nm. The overall chemical composition of the particles during the different reaction steps is monitored by quantitative Al Kα excitation X-ray photoelectron spectroscopy (XPS). Here, the formation of stoichiometric metal fluorides (MF$_2$) is confirmed, both for the core and the final core–shell particles. Furthermore, an in-depth analysis by synchrotron radiation XPS (SR-XPS) with tunable excitation energy is performed to confirm the core–shell character of the nanoparticles. Additionally, Ca2p/Sr3d XPS intensity ratio in-depth profiles are simulated using the software Simulation of Electron Spectra for Surface Analysis (SESSA). In principle, core–shell like particle morphologies are formed but without a sharp interface between calcium and strontium containing phases. Surprisingly, the in-depth chemical distribution of the two types of nanoparticles is equal within the error of the experiment. Both comprise a SrF$_2$-rich core domain and CaF$_2$-rich shell domain with an intermixing zone between them. Consequently, the internal morphology of the final nanoparticles seems to be independent from the synthesis chronology.

KEYWORDS
metal fluorides, nanoparticles, sol–gel synthesis, synchrotron radiation, X-ray photoelectron spectroscopy

1 | INTRODUCTION

Metal fluoride nanoparticles gained more and more interest in luminescence applications in the last years. They are chemically more stable than metal chlorides and bromides, have a higher band gap than metal sulfides or selenides, and possess lower phonon energies than metal oxides, resulting in higher quantum yields. These properties make them suitable for doping with luminescent rare-earth metal ions. By appropriate choice of the rare-earth metal ions, tuning of the excitation and emission wavelength is possible, yielding particles capable of photon down-conversion or up-conversion.[1-3] Even though the most commonly used matrix compound is β-NaYF$_4$ and its relatives, recently, the alkaline earth metal fluorides CaF$_2$ and SrF$_2$ proved to be interesting matrix compounds for rare-earth metal ions, as well.[4-8] The luminescence properties of such nanoparticles can be improved by performing the synthesis in a stepwise manner: The first fluorination is supposed to yield lanthanide-doped nanoparticles; the second fluorination is meant to encapsulate them by a protective undoped alkaline earth metal fluoride shell.[9-13]

Serious obstacles for the production of nanoparticles for actual applications are high costs and low yields. The fluorolytic sol–gel synthesis is an elegant method to obtain larger amounts of metal fluoride nanoparticles up to the kilogram scale.[14-16] Here, an appropriate metal precursor is reacted with anhydrous HF, and transparent water-clear dispersions in alcohol are obtained. Doping of the particles with rare-earth metal ions results in extraordinary luminescence properties.[8,13,17] Recently, this method was extended to the design of tailor-made core–shell systems based on CaF$_2$ and SrF$_2$, allowing the stepwise synthesis of a rare-earth metal ion-doped core encapsulated by differently doped or undoped shells.[13] The core–shell particle morphology formation was deduced indirectly from an analysis of the nanoparticles' luminescence properties. Furthermore, ^{19}F nuclear magnetic resonance (NMR) spectroscopy reveals different signals from Ca-rich and Sr-rich domains probably located at the surface and center of the particle and an intermixing domain presumably located between them.

In the present work, the fluorolytic sol–gel synthesis is applied with the intention to obtain two different types of core–shell nanoparticles, namely, SrF$_2$–CaF$_2$ and CaF$_2$–SrF$_2$. Laboratory-based Al Kα excitation X-ray photoelectron spectroscopy (XPS) is used to monitor the overall chemical composition of the particles during each step of the synthesis. Furthermore, in-depth analysis by synchrotron radiation XPS (SR-XPS) in combination with scanning transmission electron microscopy (STEM) is applied, in order to obtain more direct and detailed information about the internal morphology of the nanoparticles. Due to the significant photo- and Auger-emission of most lanthanides in the 0 to 700 eV binding energy range at Al Kα excitation, the synthesis of undoped nanoparticles is investigated that serve as model systems for their lanthanide-doped counterparts. Thereby, overlapping with Ca2p and Sr3d signals is avoided, and the quantification of the alkaline earth metals can be performed with higher accuracy.

XPS is a very powerful tool for the characterization of nanoparticles and nanoparticle coatings due to its outstanding surface sensitivity combined with an element specific sensitivity down to 0.1 at%.[18] The importance of the method for this field is underlined by the number of articles and book chapters that have been published in recent years.[19-28] These publications not only report great advances but also point out the numerous challenges that must be considered in order to produce meaningful results with an XPS analysis of nanoparticles and nanoparticle coatings.

SR-XPS has been successfully applied in the past to investigate the internal heterostructure of nanoparticles.[29-32] The variability of the photon energy leads to a variability of the kinetic energy of the photoelectrons. Meanwhile, the adjustment of the kinetic energy refers to an adjustment of the inelastic mean free path (IMFP) and, consequently, the z_{95} information depth[33,34] of the photoelectrons. Therefore, a profile of the in-depth chemical composition can be obtained. This principle is particularly interesting for the analysis of nanoparticles, because the surface geometry of a nanoparticle powder differs to such a great extent from a flat surface that depth profiling by angle-resolved XPS becomes impossible. In this work, we provide a detailed and complete description of the data acquisition and analysis process necessary to obtain a profile of the in-depth chemical composition of the investigated alkaline earth metal fluoride nanoparticles. To the best of our knowledge, this is the first time that this kind of depth-profiling by XPS is applied to nanoparticles considering the impact of the following two factors on the photoionization cross sections: (I) the linear polarization of the synchrotron light and (II) the anisotropy of the photoelectrons' angular distribution for orbitals with an angular quantum number $l \neq 0$.

SR-XPS indeed confirms the formation of core–shell like particle morphologies. However, the scenario of a sharp interface between core and shell material can be clearly disproved by STEM. Surprisingly, the internal morphology of the final nanoparticles is equal, no matter whether the synthesis was started with the fluorination of calcium or strontium lactate. In both cases, they comprise a SrF$_2$-rich core domain and a CaF$_2$-rich shell domain with an intermixing zone between them. Consequently, the chronology of the synthesis seems to be irrelevant for the internal morphology of the final nanoparticles.

Furthermore, in order to support the interpretation of the SR-XPS results, Ca2p/Sr3d XPS intensity ratio in-depth profiles were simulated for different morphologies and distributions of Ca and Sr in the nanoparticles using the software "Simulation of Electron Spectra for Surface Analysis" (SESSA) Version 2.1.1.[35] These simulated in-depth profiles underpin the scenario of a Ca enrichment at the surface of the nanoparticles. In order to make these complex simulations reproducible for other scientists, the Supporting Information of this article contains the complete SESSA input scripts as well as a Phyton program that sorts the SESSA output into a convenient table.

2 | EXPERIMENTAL SECTION

2.1 | Reagents

Calcium lactate hydrate (AppliChem) and strontium lactate hydrate (Paul Lohmann GmbH) were dehydrated at 80°C in vacuum

for 8 h. Water content of the dehydrated compounds was determined by thermogravimetric analysis (Ca $(OLac)_2 \cdot 0.424H_2O$, Sr $(OLac)_2 \cdot 1.007H_2O$). Ethylene glycol (99.5%) was obtained from Carl Roth GmbH.

Methanolic HF was manufactured by bubbling gaseous HF diluted with argon through anhydrous methanol in an FEP bottle. The exact HF content was determined by titration with NaOH. The complete procedure is described elsewhere.[36] Caution: HF is a hazardous agent and has to be used under restricted conditions only.

2.2 | Particle synthesis

2.2.1 | Core particles CaF_2 (≕Ca–Sr(2)) and SrF_2 (≕Sr–Ca(2))

Polypropylene beakers and pipettes were used for the synthesis. For CaF_2, 9.035 g Ca $(OLac)_2 \cdot 0.424H_2O$ (40.0 mmol) were dissolved in 190 mL ethylene glycol (≕Ca–Sr(1)). Under vigorous stirring, 3.45 mL of 23.2 M anhydrous HF (80.0 mmol) dissolved in methanol was added. After 20 min of stirring, a transparent water-clear sol was obtained (≕Ca–Sr(2)). For SrF_2, 11.357 g Sr $(OLac)_2 \cdot 1.007H_2O$ (40.0 mmol) were used instead of Ca $(OLac)_2$. The total volume after reaction was 200 mL; the concentration of CaF_2 or SrF_2, respectively, was 0.2 M.

2.2.2 | Ca–Sr(3) and Ca–Sr(4)

To 30 mL of the synthesized CaF_2 sol, containing 6.0 mmol CaF_2, 1.704 g Sr $(OLac)_2 \cdot 1.007H_2O$ (6.0 mmol) was added. After 10 min of stirring, a transparent clear reaction mixture was obtained (≕Ca–Sr(3)). Under vigorous stirring, 0.52 mL of 23.2 M HF/MeOH was added. After 30 min of stirring, the reaction mixture was transparent and water-clear (≕Ca–Sr(4)).

2.2.3 | Sr–Ca(3) and Sr–Ca(4)

To 30 mL of the synthesized SrF_2 sol, containing 6.0 mmol SrF_2, 1.335 g Ca $(OLac)_2 \cdot 0.424H_2O$ (6.0 mmol) was added. After 10 min of stirring, a transparent clear reaction mixture was obtained (≕Sr–Ca(3)). Under vigorous stirring, 0.52 mL of 23.2 M HF/MeOH was added. After 30 min of stirring, the reaction mixture was transparent and water clear (≕Sr–Ca(4)).

For comparison, a second batch was prepared, named Ca–Sr(4)-II and Sr–Ca(4)-II. Furthermore, 20 mL of the reaction mixture was removed at each step of the synthesis procedure for subsequent analysis. From this 20 mL fraction, 100 μL were purified by repeated dialysis as described below.

2.3 | Purification by dialysis

100 μL of nanoparticle suspension were diluted with methanol (gradient grade for high-performance liquid chromatography [HPLC], min. 99.85%) purchased from TH.GEYER (Renningen, Germany) by a factor of 50. Dialysis tubing with a molecular weight cutoff (MWCO) of 12–14 000 Daltons purchased from Medicell International Ltd. (London, UK) was used. The pore size is approximately 2.5 nm; 5 mL of nanoparticle suspension were filled into the dialysis tubing, and the sealed tubing was inserted into a beaker with 400 mL methanol, which was continuously stirred. The beaker was sealed by parafilm to avoid evaporation of the solvent during the purification process. The surrounding solvent was entirely exchanged after 2 h, 4 h, 6 h, 3 days, and 4 days. After 5 days, the dialysis was finished by removing the filled tubing from the beaker. If samples in this paper are labeled as "purified", such samples were prepared from the nanoparticle suspensions after 5 days of dialysis.

2.4 | Sample preparation for XPS

1.0×1.0 cm^2 (100) silicon wafers were purified by consecutive sonication in 2% aqueous Hellmanex III solution, isopropyl alcohol, and ethanol. After drying the wafers using a nitrogen spray gun, their surface was treated for 20 min using an ultraviolet (UV) Ozone Cleaner UVC-1014 (185 and 254 nm wavelength UV radiation source) manufactured by NanoBioAnalytics (Berlin, Germany). A 5-μL drop of the purified nanoparticle suspension was drop-casted onto the wafer surface and dried for 15 min at 100°C. Drop-casting of 5 μL suspension onto the same spot on the wafer and subsequent heating are performed three times in total.

The samples Sr–Ca(1) and Ca–Sr(1) that contain exclusively the alkaline earth metal ions in ethylene glycol were not investigated, because the concentration of these solutions was too low for XPS investigation. Instead, saturated aqueous solutions of pure strontium and calcium lactate were prepared. A single 20 μL drop of each saturated solution was deposited onto a wafer and left to dry at air. The wafer surface had been priorly purified as described above but not treated using the UV Ozone Cleaner. These samples were used for all XPS measurements performed in this paper labeled with Sr–Ca(1) and Ca–Sr(1).

2.5 | Al Kα excitation XPS

All measurements were performed with an AXIS Ultra DLD photoelectron spectrometer manufactured by Kratos Analytical (Manchester, UK). XPS spectra were recorded using monochromatized Al Kα radiation for excitation, at a pressure of approximately 5×10^{-9} mbar. The electron emission angle was 0°, and the source-to-analyzer angle was 60°. The binding energy scale of the instrument was calibrated following a Kratos Analytical procedure, which uses ISO 15472 binding energy data.[37] Spectra were taken by setting the instrument to the hybrid lens mode and the slot mode providing approximately a 300×700 $μm^2$ analysis area. Furthermore, measurements were performed in fixed analyzer transmission (FAT) mode.

Survey spectra were recorded with a step size of 1 eV and a pass energy of 80 eV; high-resolution spectra were recorded with a step size of 0.1 eV and a pass energy of 20 eV. The charge neutralizer was used to compensate and stabilize the surface charge of the wafer with deposited sample mounted without grounding. Peak fitting and quantification of the recorded spectra were performed using the Software UNIFIT-2020.[38] Because correction of the XPS peak areas by conventional standard-free sensitivity factors was found to be insufficiently accurate in this case, new sensitivity factors were determined empirically using the pure metal lactates Sr–Ca(1) and Ca–Sr(1) as reference materials (see Section 1.1-2 of the Supporting Information). Survey spectra of the dialyzed suspensions are depicted in Figure 3, and the results from their quantification can be found in Section 1.3 of the Supporting Information. A full set of fitted high-resolution spectra and associated fitting parameters can be found in Section 1.4 of the Supporting Information.

2.6 | Synchrotron radiation XPS

All measurements were carried out with a Scienta R3000 electron energy analyzer at the endstation of the high energy-spherical grid monochromator (HE-SGM) dipole magnet beamline at the BESSY II SR source (Berlin, Germany). A schematic representation of the experimental geometry can be found in Figure S5. High-resolution core-level spectra of the Sr3d and the Ca2p photoelectron signals were recorded in FAT mode at a pass energy of 50 eV and a step size of 0.1 eV. For Sr3d excitation, energies of 235, 335, 435, and 535 eV were selected, while for Ca2p, 449, 549, 649, and 749 eV were applied. Therefore, the Sr3d and Ca2p photoelectrons exhibited kinetic energies of 100, 200, 300, and 400 eV, which corresponds to a z_{95} XPS information depth between 2.3 and 4.5 nm. Because the synchrotron facility was operated in top-up mode, deviations in light intensity due to the ring current are negligible. The ideal orientation of the mirror guiding the beam from the ring through the beamline towards the spectrometer and, thus, ensuring maximum light intensity was controlled by using a gold grid mounted in the beamline for monitoring the current I_0.

In order to determine the chemical composition of the samples, the XPS experimental peak intensities were normalized by asymmetry corrected photoionization cross sections and the HE-SGM monochromator transmission function. These two quantities are functions of the photon energy. More detailed information about the monochromator transmission function as well as about the asymmetry correction of the photoionization cross sections for linearly polarized synchrotron light can be found in Section 2.1 of the Supporting Information. A normalization by the spectrometer transmission function and the *IMFP* was not required, because the constant kinetic energy XPS method was applied.[34] A full set of fitted high-resolution spectra, the corresponding fitting parameters, and a tabulation of SR-XPS results can be found in Section 2.2 of the Supporting Information.

2.7 | Calculation of the XPS information depth

In this work, the z_{95} information depth is defined as three times the *IMFP* of the photoelectrons; 95% of the photoelectrons that contribute to the XPS intensity originate from this depth range.[33,34] The *IMFP* was calculated based on the TPP-2M formula by Tanuma et al.[39] Elastic-electron scattering effects have been neglected. For Al Kα excitation XPS, photoelectrons of 801, 1138, and 1352 eV kinetic energy referring to F1s, Ca2p, and Sr3d, respectively, were considered. Two separate *IMFP* calculations were performed for each of these photoelectrons traveling through calcium fluoride, on the one hand, and through strontium fluoride, on the other hand. For the SR-XPS, photoelectrons of 100, 200, 300, and 400 eV kinetic energy were considered. Two separate *IMFP* calculations were performed for each of these photoelectrons traveling through calcium fluoride, on the one hand, and through strontium fluoride, on the other hand. The z_{95} results from these two calculations were averaged for each of the four kinetic energies.

2.8 | ICP-MS

Only the solvent surrounding the tubing during the dialysis of Sr–Ca (4)-II and Ca–Sr(4)-II was investigated. Prior to exchange of the solvent after 2 h, 4 h, 6 h, and 3 days, always a 10 mL fraction was removed for inductively coupled plasma mass spectrometry (ICP-MS) analysis. These fractions were diluted by a factor of 50 with ultrapure water. The measurements were performed with the Element 2 high-resolution ICP-MS instrument manufactured by Thermo Fisher Scientific Inc. (Waltham, Massachusetts, USA). A 1 μg/L aqueous solution of the B, Ba, Ce, Co, Fe, Ga, In, K, Li, Lu, Na, Rh, Sc, Tl, U, and Y was prepared from single element standard solutions purchased from Merck (Darmstadt, Germany). Na, In, and U were used for optimization of the signal intensities. The same solution was used for calibration of the mass scale. Every time the tube to the ICP-MS instrument was changed from one sample to another sample, it was repeatedly rinsed by ultrapure water and 1 vol% aqueous HNO_3. Measurements were performed both in "medium resolution" and "high resolution" mode. No internal standard was used. The detection limit of the measurement was approximately 0.03 μg/L for Sr and 0.3 μg/L for Ca ions.

2.9 | Sample preparation for STEM

Only the samples Sr–Ca(4)-II and Ca–Sr(4)-II were investigated by STEM. The suspensions were purified by dialysis as described above. Afterwards, they were further diluted by a factor of 200. 5 μL were deposited onto a 0.5 × 0.5 mm broad and 100-nm-thick silicon nitride window in a 200 nm thick round silicon frame with 3 mm diameter manufactured by Norcada Inc. (Edmonton, Canada). The samples were stored at a pressure of 5×10^{-5} mbar for 4 days, in order to remove all solvent residues.

2.10 | Scanning transmission electron microscopy

STEM measurements were performed in scanning mode in a JEOL (Tokyo, Japan) JEM ARM200F electron microscope equipped with a probe Cs corrector using the annular bright field (ABF) and high-angle annular dark field (HAADF) detectors for electron signal detection. Additional analytical data for determining local compositions were acquired with the attached energy dispersive X-ray (EDX) spectrometer JEOL JED2300.

2.11 | Dynamic light scattering

Dynamic light scattering (DLS) was measured on a Zetasizer Nano in PMMA cuvettes using a 630 nm light source. The viscosity of each sol was determined separately for evaluation.
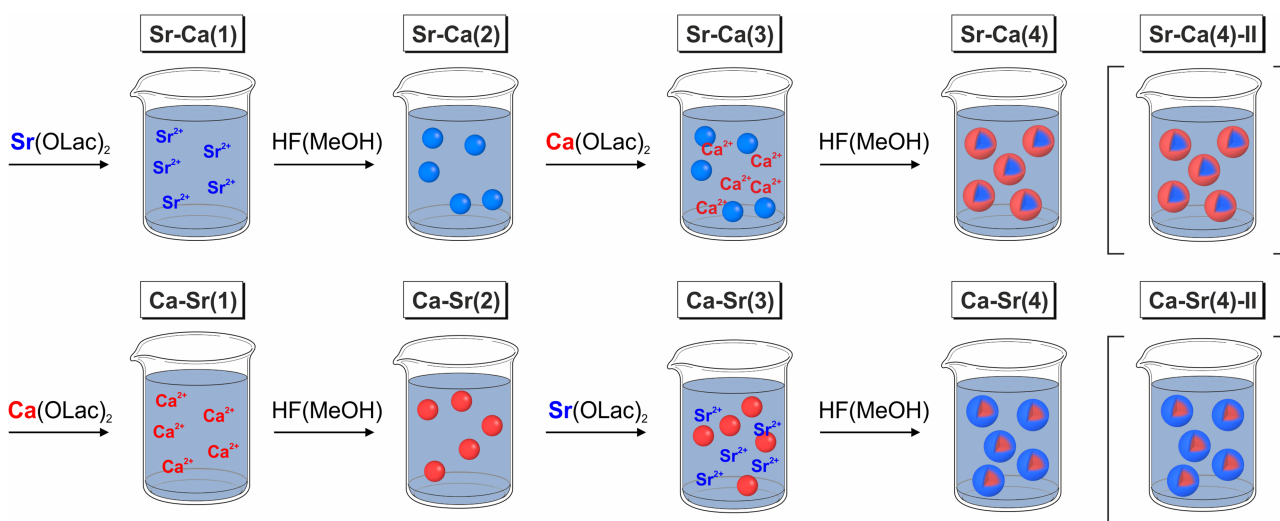
3 | RESULTS

The aim of the synthesis was obtaining two different types of core–shell particles, namely, a SrF_2 core surrounded by a CaF_2 shell and vice versa. Briefly, core nanoparticles are synthesized by dissolving the corresponding metal lactate in ethylene glycol (Step 1) followed by fluorination with anhydrous HF (Step 2), yielding a transparent dispersion of alkaline earth metal fluoride nanoparticles. Subsequently, the other metal lactate is dissolved in this nanoparticle dispersion (Step 3) and fluorinated again (Step 4). The two nanoparticle synthesis procedures used in this study are schematically depicted in Figure 1. The different steps of the nanoparticle synthesis started with strontium lactate will in the following be referred to as Sr–Ca(1)–(4), and the different steps of the nanoparticle synthesis started with calcium lactate as Ca–Sr(1)–(4). The first synthesis of the nanoparticles performed in

January 2016 was replicated in January 2019. In 2019, all four steps of the synthesis were investigated, while in 2016, only the final step was considered. The samples from 2016 will be referred to as Sr–Ca (4)-II and Ca–Sr(4)-II.

A 20 mL fraction was removed from the solutions or suspensions at each step of the synthesis (cf. Figure 1) for subsequent analysis by XPS; 100 μL of this fraction were purified by repeated dialysis as described in the experimental section. This purification step is supposed to remove all free-floating Sr^{2+}, Ca^{2+}, F^-, and $C_3H_5O_3^-$ ions from the suspensions, while the nanoparticles remain. Furthermore, the solvent ethylene glycol used for nanoparticle synthesis should be entirely exchanged by methanol. Only for the samples Sr–Ca(1) and Ca–Sr(1), no purification by dialysis was performed, because no nanoparticles are formed, yet, at this stage of the synthesis. Therefore, no differentiation between nanoparticles and free-floating species is required.

3.1 | ICP-MS

ICP-MS was applied to confirm that the purification by dialysis was complete. In other words, it should be proved that the solution surrounding the dialysis tubing is free from Ca^{2+} and Sr^{2+} ions in the end of the purification process. This is of importance, because XPS cannot distinguish calcium and strontium in the nanoparticles from residues originating from free-floating calcium and strontium ions in solution. Only the solvent surrounding the tubing during the dialysis of Sr–Ca(4)-II and Ca–Sr(4)-II was investigated. Prior to the exchange of the solvent after 2 h, 4 h, 6 h, and 3 days, a 10 mL fraction was removed for ICP-MS analysis. In none of these samples, any Ca^{2+} or Sr^{2+} ions could be detected. Consequently, the measured calcium and strontium XPS intensities originate from the nanoparticles exclusively.


FIGURE 1 Schematic representation of the anticipated Sr–Ca synthesis (upper row) and the Ca–Sr synthesis (lower row). The suspensions resulting from the different steps of the synthesis started with $Sr(OLac)_2$ are referred to as Sr–Ca(1)–(4), and suspensions resulting from the different steps of the synthesis started with $Ca(OLac)_2$ are referred to as Ca–Sr(1)–(4). OLac = lactate

3.2 | STEM and DLS

STEM experiments were performed, firstly, in order to characterize size and shape of the nanoparticles and, secondly, to determine the distribution of calcium and strontium in individual nanoparticles. Only the samples Sr–Ca(4)-II and Ca–Sr(4)-II were investigated after purification by dialysis. Figure 2C–F shows STEM micrographs of two different magnifications recorded in HAADF mode. Further micrographs recorded in HAADF mode can be found in Section 3 of the Supporting Information. Remaining carbohydrates attached to the specimen were cracked during irradiation under the electron beam leading to amorphous carbon contamination growth during the imaging process and, therefore, inhibiting the quality of the images.

The particles of both samples are not spherical. The majority exhibits an elongated, ellipsoidal shape. With increasing diameter additionally, rhomboid- and hexagon-shaped particles are observed. In the case of the Sr–Ca(4)-II sample, even a very small proportion of needle-shaped particles was found. The crystallinity of the particles is confirmed by the appearance of lattice planes in the HAADF-STEM micrographs. The observed plane spacings are in good agreement with the values for the 111, 200, and 220 lattice planes of CaF_2 and SrF_2. However, the difference between the plane spacings of CaF_2 and SrF_2 from literature is at maximum 0.2 Å. This is within the uncertainty of the given STEM measurements, and thus, the observed lattice plane spacings cannot be used to reliably differentiate CaF_2, SrF_2, or mixed fluorides $Ca_xSr_{1-x}F_2$. A distinct core–shell morphology with a sharp interface between CaF_2 and SrF_2 domains at the surface and in the center of the particles, respectively, could not be identified during the STEM analysis. However, the crystallites show local variations in composition with a tendency following the preparation
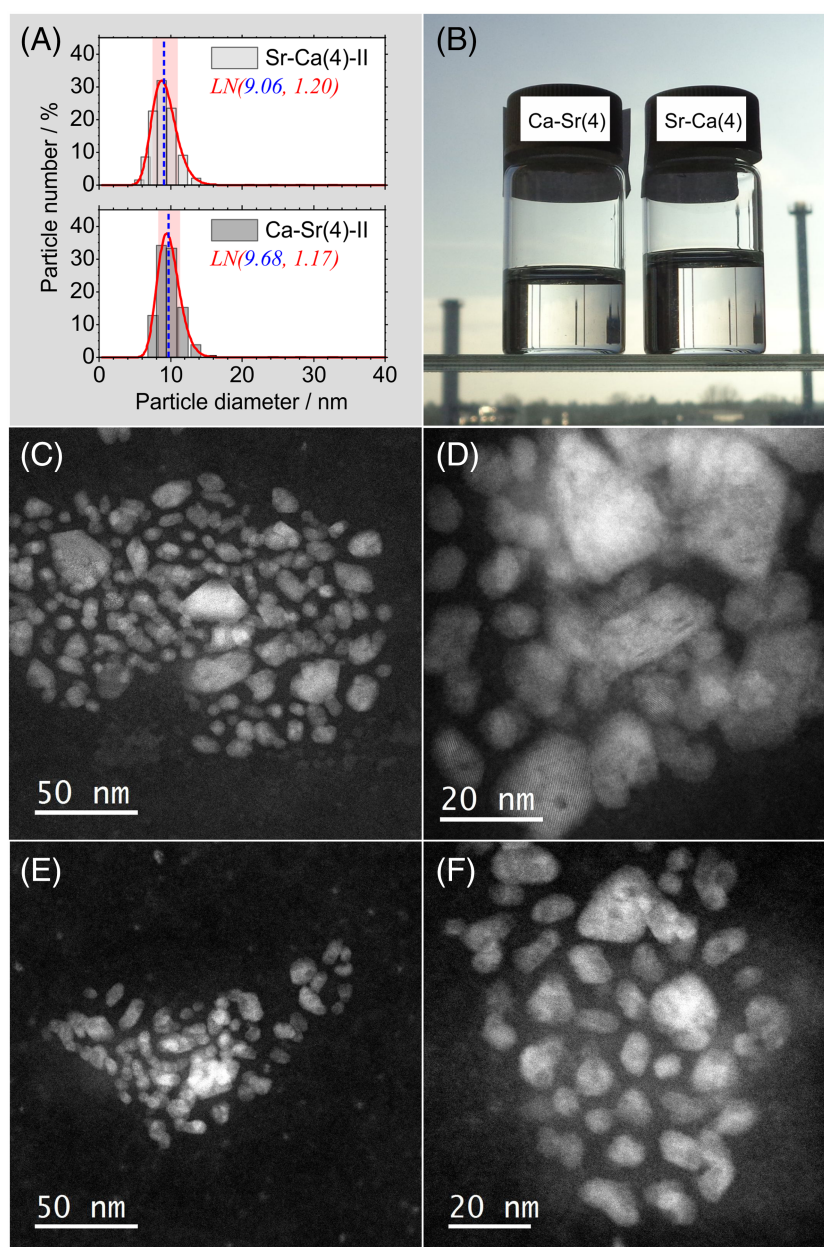

FIGURE 2 (A) Dynamic light scattering (DLS) data of the samples Sr–Ca(4)-II and Ca–Sr(4)-II. The particle diameter histograms from DLS were fitted with logarithmic normal distributions $LN(\mu^*,\sigma^*)$. see section 3 of the Supporting Information for further details on $LN(\mu^*,\sigma^*)$. (B) Photograph of the nanoparticle suspensions of the samples Sr–Ca(4) and Ca–Sr(4) in ethylene glycol. High-angle annular dark field (HAADF) mode scanning transmission electron microscopy (STEM) micrographs of the sample Sr–Ca(4)-II (C,D) and Ca–Sr(4)-II (E,F). Local bright contrast indicates the presence of the heavier element strontium within a particle

procedure regarding which element can be found predominantly at the surface especially in the case of Ca–Sr(4)-II.

Furthermore, nanoparticle sizes could be determined from STEM. Low image contrast and strong agglomeration of the nanoparticles render an automatized analysis of the micrographs impossible. Therefore, the analysis was performed manually. Due to the elongated shape of the particles, both the maximum and the minimum diameter of each particle were measured. For sample Sr–Ca(4)-II, 11.5 (7.6–17.7) and 8.0 (5.6–11.3) nm were determined as average maximum and minimum diameter, while for sample Ca–Sr(4)-II, 9.6

(6.9–13.4) and 6.4 (4.9–8.4) nm were found. The values in parentheses indicate the standard deviation interval, which contains ∼68% of all data. Note that the needle-shaped particles in the Sr–Ca(4)-II sample were not included in the size measurement. Due to their very small number, they were considered statistically irrelevant. The good agreement between STEM and DLS results supports this assumption.

Furthermore, nanoparticle diameter distribution histograms from DLS analysis can be found in Figure 2A. The histograms were fitted with logarithmic normal distributions (red lines). The dashed blue line is the median, and the transparent red area indicates the standard
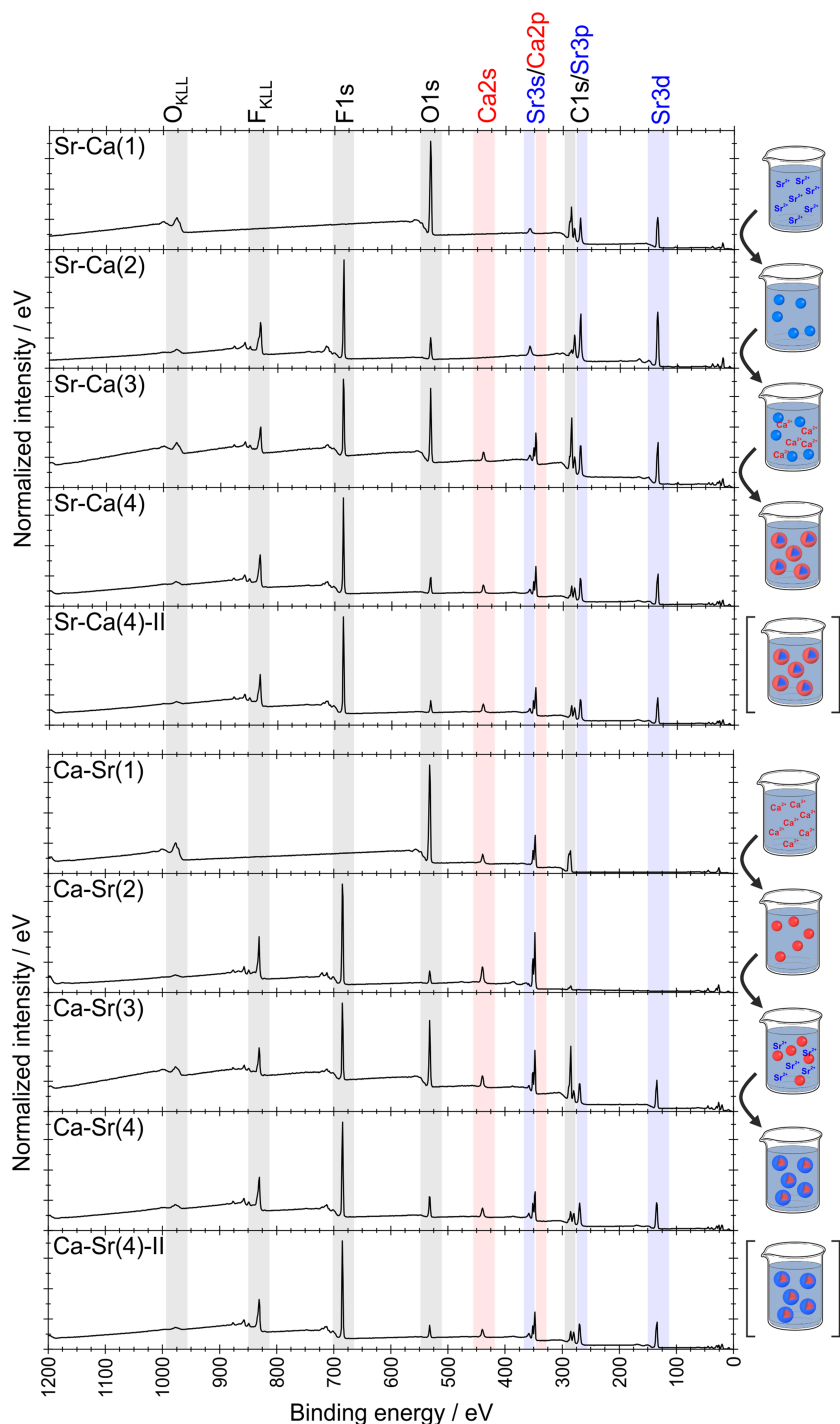
FIGURE 3 X-ray photoelectron spectroscopy (XPS) survey spectra of the samples Sr–Ca(1)–(4) and Sr–Ca(4)-II as well as Ca–Sr(1)–(4) and Ca–Sr(4)-II recorded at the KRATOS AXIS ultra DLD photoelectron spectrometer with monochromatized Al Kα excitation and energy referenced relative to the aliphatic carbon C1s component at 285.0 eV. Only spectra of the dialyzed suspensions are presented in this figure

deviation interval of the distribution with ∼68% of all particle diameters. DLS yields an average diameter of 9.1 (7.5–10.9) nm for Sr–Ca (4)-II and 9.7 (8.3–11.3) nm for Ca–Sr(4)-II. Within the error of the experiment, the diameters from DLS analysis agree with the diameters from STEM analysis. However, the DLS results can only be considered a rough estimate, because they are based on the model of a perfect sphere, which is clearly wrong for the investigated nanoparticles. Sections 3 and 4 of the Supporting Information contain all information about the mathematics behind the logarithmic normal distribution used to fit both the STEM and the DLS nanoparticle diameter histograms.

3.3 | Chemical composition from Al Kα excitation XPS

Both the as-synthesized and the dialyzed suspensions Sr–Ca(1)–(4) and Sr–Ca(4)-II as well as Ca–Sr(1)–(4) and Ca–Sr(4)-II were investigated by laboratory-based Al Kα excitation XPS. Figure 3 comprises the survey spectra of all dialyzed suspensions. The suspensions were drop-casted onto a silicon wafer and dried for the XPS analysis, which is performed in ultra-high vacuum. Therefore, the samples contain all nonvolatile components of the suspension (both from the nanoparticles and from the surrounding solution).

Elemental fractions of carbon, oxygen, calcium, strontium, and fluorine were determined by quantification of the survey spectra. Because conventional standard-free sensitivity factors for XPS quantification were found to be insufficiently accurate in this case, new sensitivity factors were determined empirically by measuring the pure metal lactates Sr–Ca(1) and Ca–Sr(1) as reference materials (see Section 1.1-2 of the Supporting Information). The quantification results for all elements can be found in Table S5 and S6 of the Supporting Information. In the following, predominantly the relative molar amounts of calcium, strontium, and fluorine are discussed. The z_{95} XPS information depth at Al Kα excitation is between 7.6 and 11.3 nm for F1s, Ca2p, and Sr3d photoelectrons passing through CaF_2, while it is between 6.6 and 9.9 nm for the photoelectrons passing through SrF_2. Relative to the mean nanoparticle diameters of around 8.9 nm determined by STEM analysis, these XPS measurements are more bulk sensitive than surface sensitive.

Figure 4 summarizes the F/(Ca + Sr) and Ca/(Ca + Sr) molar ratios obtained both from the as-synthesized and the dialyzed suspensions at the different synthesis steps Sr–Ca(2)–(4) and Sr–Ca(4)-II as well as Ca–Sr(2)–(4) and Ca–Sr(4)-II. The error bars are based on a ±10% uncertainty of the relative molar amount of each element calcium, strontium, and fluorine. The overall uncertainty of the F/(Ca + Sr) and Ca/(Ca + Sr) ratios was calculated according to the spreadsheet technique developed by Kragten.[40]
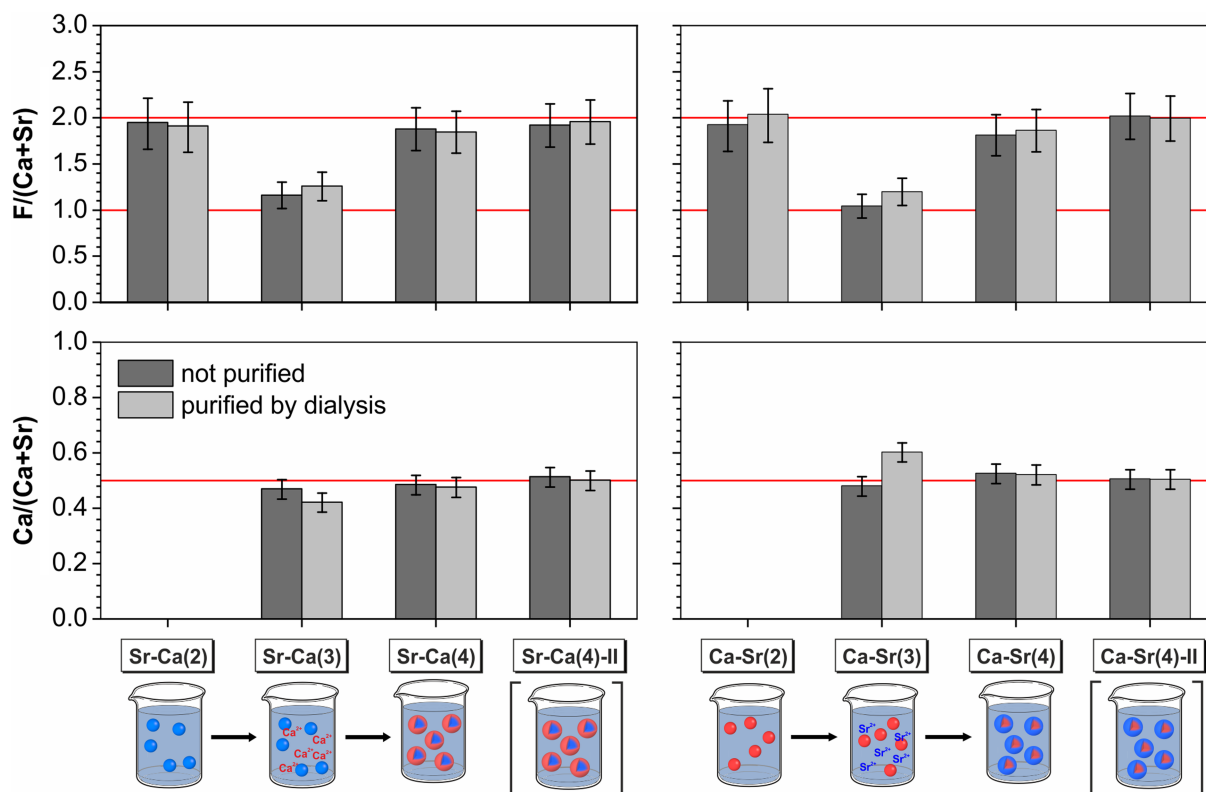
FIGURE 4 Molar ratios F/(Ca + Sr) both from the as-synthesized and the dialyzed suspensions at the different synthesis steps Sr–Ca(2)–(4) and Sr–Ca(4)-II as well as Ca–Sr(2)–(4) and Ca–Sr(4)-II (upper row). Molar ratios Ca/(Ca + Sr) both from the as-synthesized and the dialyzed suspensions at the different synthesis steps (lower row). The values were obtained from quantitative analysis of the X-ray photoelectron spectroscopy (XPS) survey spectra recorded at the KRATOS AXIS ultra DLD photoelectron spectrometer with monochromatized Al Kα excitation

3.3.1 | Steps Sr–Ca(2) and Ca–Sr(2)

At Steps Sr–Ca(2) and Ca–Sr(2) of each synthesis procedure, that is, the synthesis of the pure core particles, hydrogen fluoride and metal lactate were added at a molar ratio of 2:1, and metal fluoride nanoparticles were formed. The F/(Ca + Sr) molar ratios from XPS of the as-synthesized suspensions very well agree with the ratios that were added during the synthesis. The F/(Ca + Sr) molar ratios of the dialyzed are equal to those of the as-synthesized suspensions. As mentioned before, XPS spectra of the dialyzed suspensions exclusively contain elements present in the nanoparticles. This confirms that all metal and fluorine ions react and form stoichiometric metal fluoride (MF_2) nanoparticles. No free-floating metal ions remain in suspension.

3.3.2 | Steps Sr–Ca(3) and Ca–Sr(3)

At Steps Sr–Ca(3) and Ca–Sr (3) of each synthesis procedure, the second metal lactate was added at a molar ratio of 1:1 relative to the metal lactate added in the previous step. Before and after purification by dialysis, both calcium and strontium are detected (see Figure 3). Consequently, the second metal ion must already be part of the nanoparticles at this stage, because the dialysis removes all metal ions in solution.

The Ca/(Ca + Sr) molar ratios of approximately 0.5 from XPS of the as-synthesized suspensions are equal to the molar ratios that were added during the synthesis. After dialysis, the Ca/(Ca + Sr) ratios reflect the extent at which each metal ion was incorporated into the nanoparticles. In the case of Sr–Ca(3), an excess of strontium is detected, while for Ca–Sr(3), an excess of calcium is observed. Consequently, the alkaline earth metal ion used to start the synthesis is incorporated to a greater extent, respectively. Due to the high amount of alkaline earth metal relative to fluorine at this step of the synthesis, the metal ion added subsequently cannot fully react anymore. A fraction of the metal ions, consequently, remains in solution and is removed during the purification by dialysis. Tables S5 and S6 confirm that the difference in Ca/(Ca + Sr) molar ratio between the as-synthesized and the purified suspension is predominantly caused by removal of the subsequently added metal ion, respectively.

Furthermore, during this step of the synthesis, the particles contain about 6 times more carbon and oxygen than in all other synthesis steps (see Figure 3 and Tables S5 and S6), which cannot be removed during dialysis. This can also be explained by the exceptionally high amount of metal relative to fluorine at this synthesis step. Obviously, the major part of the added metal lactate already strongly interacts with the metal fluoride nanoparticles, most probably due to interaction with the particle surface and beginning cation exchange. Thus, the majority of the lactate is immobilized at the particles together with solvate molecules and, hence, will not penetrate the dialysis membrane.

The F/(Ca + Sr) molar ratio added during synthesis is 1. The F/(Ca + Sr) molar ratios from XPS of the as-synthesized suspensions agree with this value. Because metal ions are removed during purification by dialysis, the F/(Ca + Sr) of the dialyzed suspensions is higher than the ratio of the as-synthesized suspensions. However, in contrast to the previous step of the synthesis, the theoretical F/(Ca + Sr) ratio of 2 for stoichiometric MF_2 nanoparticles is not found after purification of the suspension by dialysis. Consequently, the nanoparticles cannot consist of MF_2 alone, but additional metal ions are present presumably organized in a surface layer.

3.3.3 | Steps Sr–Ca(4) and Ca–Sr(4)

At Steps Sr–Ca(4) and Ca–Sr(4) of each synthesis procedure, further hydrogen fluoride was added at a molar ratio of F/(Ca + Sr) = 2 relative to the previously added alkaline earth metal ions. The F/(Ca + Sr) ratios from XPS agree with the ratio applied during synthesis within the error of the experiment. Consequently, the amount of metal relative to fluorine atoms returns approximately to the level of step Sr–Ca(2) and Ca–Sr(2) of the synthesis. Results from the dialyzed are equal to the results from the as-synthesized suspensions. The same applies to the Ca/(Ca + Sr) ratios. This means that the excess of either strontium or calcium, respectively, in the nanoparticles observed during Step (3) of the synthesis has disappeared. This observation is confirmed by analysis of the replicate samples Sr–Ca (4)-II and Ca–Sr(4)-II.

3.4 | Al Kα excitation XPS peak shape and binding energy analysis

For a binding energy and peak shape analysis, XPS high-resolution spectra of Ca2p, Sr3d, and F1s photoemission from the dialyzed nanoparticle suspensions were recorded using laboratory-based XPS at monochromatized Al Kα excitation. Spectra were acquired, both for the Sr–Ca and the Ca–Sr synthesis routes at all four steps indicated in Figure 1 and can be found in Section 1.4 of the Supporting Information.

All high-resolution spectra seem to have symmetric peak shapes. The binding energy scale of the high-resolution spectra was energy referenced relative to the aliphatic carbon C1s component at 285.0 eV. The black dots in Figure 5 represent the calibrated binding energies of the Ca2p$_{3/2}$, Sr3d$_{5/2}$, and F1s signals of the samples Sr–Ca (1)–(4) and Sr–Ca(4)-II as well as Ca–Sr(1)–(4) and Ca–Sr(4)-II. A measurement uncertainty of ±0.2 eV is indicated by the error bars.[41] The light and dark gray areas represent binding energies from literature of 347.9 and 684.8 eV for Ca2p$_{3/2}$ and F1s in CaF_2 as well as 133.9 and 684.6 eV for Sr3d$_{5/2}$ and F1s in SrF_2, also with an uncertainty of ±0.2 eV.[42,43]

While the binding energy difference between Sr3d$_{5/2}$ in strontium lactate (Sr–Ca(1)) and strontium fluoride of 0.1 eV is vanishingly small, the difference between Ca2p$_{3/2}$ in calcium lactate (Ca–Sr(1)) and calcium fluoride of 0.6 eV is more significant. At all following steps of the nanoparticle synthesis, the binding energies of Ca2p$_{3/2}$, Sr3d$_{5/2}$, and F1s are in good agreement with the binding energies

FIGURE 5 F1s, Ca2p$_{3/2}$, and Sr3d$_{5/2}$ binding energies of the samples Sr–Ca(1)–(4) and Sr–Ca(4)-II as well as Ca–Sr(1)–(4) and Ca–Sr(4)-II. Energy referencing was performed relative to the aliphatic carbon C1s component at 285.0 eV. The bright and dark gray areas indicate binding energy reference values from literature
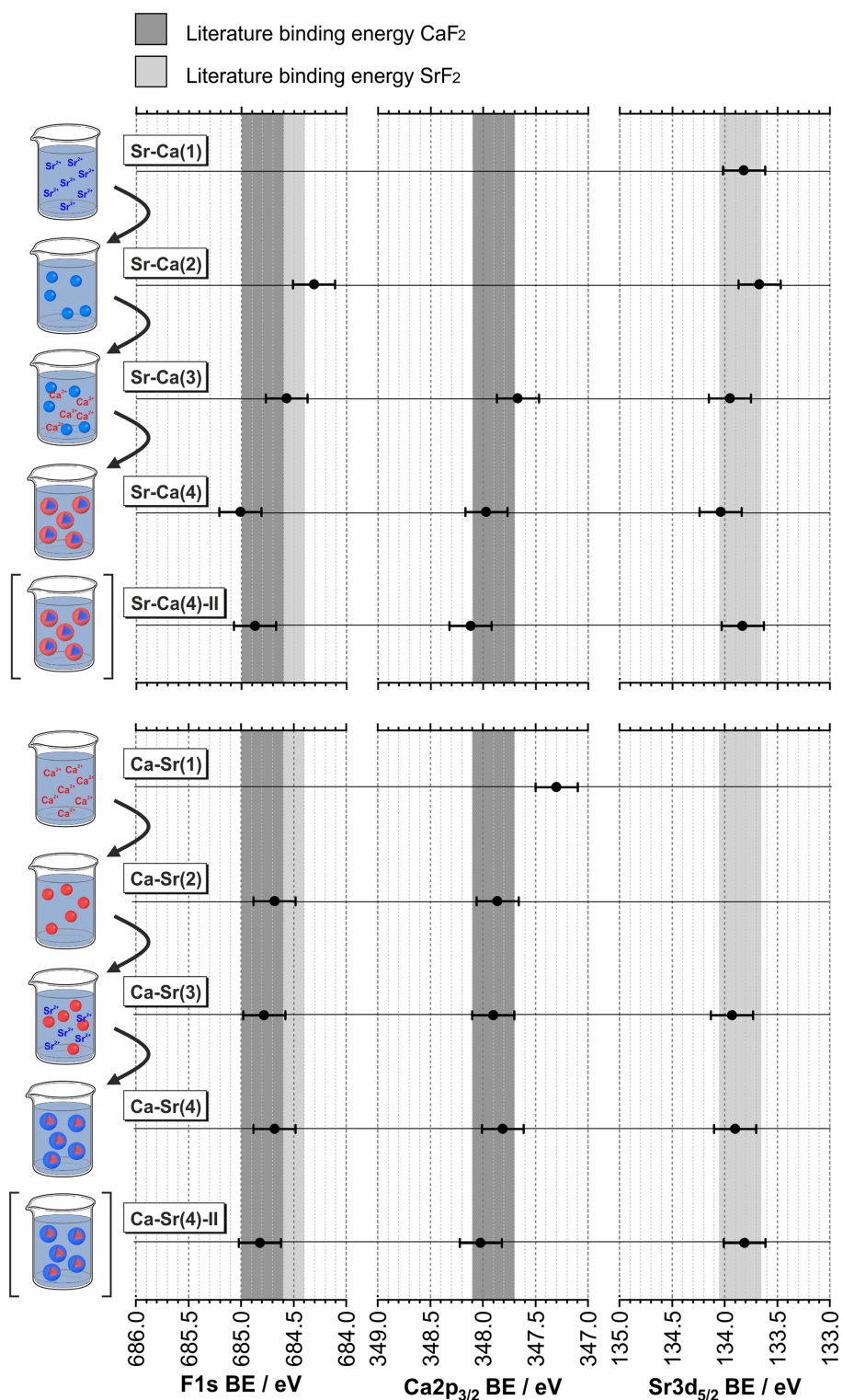
from literature for calcium and strontium fluoride. However, the Ca2p$_{3/2}$ signal of sample Sr–Ca(3) is slightly shifted towards lower binding energies compared with Sr–Ca(4) and Sr–Ca(4)-II. The lower binding energy indicates a higher amount of calcium lactate in the sample. This is in agreement with the quantification results from the previous section, where 6 times more carbon and oxygen were found for Sr–Ca(3) compared with the other synthesis steps.

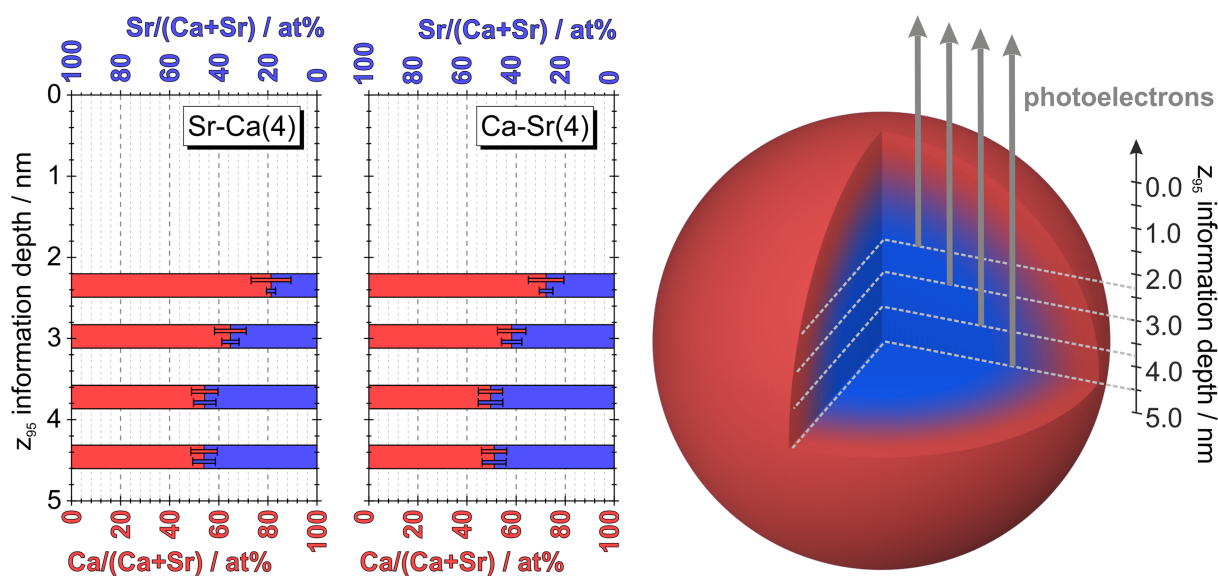## 3.5 | In-depth analysis of the samples Sr–Ca(4) and Ca–Sr(4) by SR-XPS

In contrast to laboratory-based X-ray sources that may provide two discrete characteristic X-ray photon energies (e.g., Al Kα and Mg Kα radiation), a SR source enables a continuous variation of the photon energy. A variation of the excitation energy means a variation of the

z_{95} XPS information depth and, therefore, allows for a determination of the in-depth chemical composition. This is particularly interesting, because depth profiling by angle-resolved XPS at a fixed excitation energy cannot be applied to nanoparticles. All SR-XPS experiments in this work were performed at the HE-SGM monochromator dipole magnet beamline at the BESSY II SR source (Berlin, Germany), which covers the soft X-ray range between 100 and 750 eV.

SR-XPS was applied to either prove or disprove a core–shell character of the investigated nanoparticle systems. In order to simplify the quantification of the spectra and simultaneously increase the accuracy of the results, the constant kinetic energy XPS method was applied.[34] This method works by varying the photon energy such that the photo-electrons used for quantification emitted by the different elements have equal kinetic energies. For a calculation of relative molar amounts of calcium and strontium in the sample, the correction of peak intensities for the spectrometer transmission function T and the *IMFP* is not necessary when using constant kinetic energy XPS, because both quantities T and *IMFP* cancel out. However, accurate calculation of relative molar amounts still requires the normalization by the photoionization cross sections and the monochromator transmission function, because both quantities change with photon energy. Furthermore, the photo-ionization cross sections must be asymmetry corrected, because the source-to-analyzer angle is about 10° lower than the magic angle of 54.7°. Because the degree of linear polarization of the SR at the HE-SGM beamline is 91%, the asymmetry corrected photoionization cross sections were calculated according to an expression proposed by Cooper for linearly polarized synchrotron light.[44] Furthermore, photo-electron angular distribution parameters from Trzhaskovskaya et al. were used.[45] All the details of this calculation are provided in Section 2.1 of

the Supporting Information. A full set of fitted high-resolution spectra, the corresponding fitting parameters, and a tabulation of SR-XPS results can be found in Section 2.2 of the Supporting Information.

In-depth analysis was performed by recording high-resolution spectra of the Ca2p and Sr3d photoelectron signals at the four different kinetic energies 100, 200, 300 and 400 eV, which refers to a z_{95} information depth of 2.3, 3.0, 3.7 and 4.5 nm, respectively. Figure 6 displays the relative amounts of calcium and strontium in the samples Sr–Ca(4) and Ca–Sr(4) as a function of the z_{95} information depth. The blue error bars represent a ±10% uncertainty of the relative amount of strontium, while the red error bars represent a ±10% uncertainty of the relative amount of calcium. The in-depth distribution of calcium and strontium in the two samples is equal within the error of the experiment. This is remarkable, because these two samples were prepared using two different synthesis routes (see Figure 1) aiming for different products: on the one hand, SrF_2–CaF_2 core–shell nanoparticles and, on the other hand, vice versa CaF_2–SrF_2 core–shell nanoparticles. There is clearly a variation of the relative amount of the two alkaline earth metals with the analysis depth. The measurement at z_{95} = 2.3 nm shows an excess of calcium (81% for Sr–Ca(4), 72% for Ca–Sr(4)). The higher information depth of z_{95} = 3.0 nm leads to a decrease of the relative amount of calcium, but it still prevails (65% for Sr–Ca(4), 58% for Ca–Sr(4)), while at z_{95} = 3.7 and 4.5 nm, the ratio of the two alkaline earth metals becomes approximately 1 (54 and 54% for Sr–Ca(4), 50 and 51% for Ca–Sr(4)). At these latter two information depths, relative amounts of calcium and strontium are reached, which also result from an analysis using laboratory-based Al Kα excitation XPS with z_{95} information depths between 6.6 and 11.3 nm as stated in the corresponding section above.

FIGURE 6 Quantitative in-depth analysis based on the Ca2p and Sr3d peak areas of the samples Sr–Ca(4) and Ca–Sr(4) recorded using variable synchrotron radiation for excitation. The peak areas were normalized by the asymmetry corrected photoionization cross sections and the monochromator transmission function. A correction for the *IMFP* and the spectrometer transmission function is not required, because the constant kinetic energy X-ray photoelectron spectroscopy (XPS) method[34] was applied. The core–shell like sphere in this figure is an idealized representation of the investigated nanoparticles. Even though the real nanoparticles do not exhibit a spherical shape, the scheme is supposed to increase the comprehensibility of the relation between in-depth profile and particle morphology

The maximum XPS information depth used in the SR-XPS experiment is approximately half of the average nanoparticle diameter as measured by STEM. Therefore, the in-depth profiles in Figure 6 confirm that the nanoparticles of both samples Sr–Ca(4) and Ca–Sr (4) consist of a mixed fluoride $Ca_xSr_{1-x}F_2$ with an enrichment of Ca at the surface. This is unexpected, because the nanoparticles have been prepared using different synthesis routes (cf. Figure 1).

On the one hand, the STEM results have already disproved a distinct core–shell morphology with a sharp interface between core and shell material; on the other hand, the SR-XPS results confirm that the nanoparticles consist of a mixed fluoride $Ca_xSr_{1-x}F_2$ with an enrichment of Ca at the surface. In order to better understand the actual morphology including the spatial distribution of Ca and Sr within the nanoparticles, Ca2p/Sr3d XPS intensity ratio in-depth profiles based on a variety of preset spatial distributions of these elements (morphologies) were simulated using the software "Simulation of Electron Spectra for Surface Analysis" (SESSA) Version 2.1.1. In these simulations, the overall composition and the total diameter of the nanoparticles were constrained. The complete SESSA input including scripts, physical, and chemical parameters as well as nanoparticle morphologies can be found in Section 2.3 of the Supporting Information. Furthermore, the same section contains a Python program that can be used to sort the SESSA output into a convenient table.

The Ca2p/Sr3d XPS intensity ratio in-depth profile simulated for a homogeneously composed ($Ca_{0.5}Sr_{0.5}F_2$) nanoparticle (Simulation V in Figure S10) does not compare with the measured in-depth profiles at all. Even though the order of magnitude of the obtained Ca2p/Sr3d intensity ratios is equal to the experiment, their development with photon energy is the wrong way around. As opposed to this, the simulated in-depth profile based on a distinct SrF_2–CaF_2 core–shell morphology (Simulation I in Figure S10) better matches the shape of the experimental in-depth profiles. The amount of Ca continuously decreases with decreasing surface sensitivity until it remains approximately constant for the higher information depths. However, the Ca2p/Sr3d intensity ratios obtained from this model are approximately 10 times larger than the experimental results.

A compromise between these two models was found by simulating a nanoparticle with a mixed $Ca_{0.38}Sr_{0.62}F_2$ core and a 0.3-nm CaF_2 shell (Simulation II in Figure S10). The Ca/Sr ratio in the core was selected, such that the overall Ca/Sr ratio in the nanoparticle is constrained to 1. The Ca2p/Sr3d XPS intensity ratio in-depth profile based on this model also continuously decreases with decreasing surface sensitivity like in Simulation I, but at the same time, the Ca/Sr ratio values are much closer to the experimental results. However, even with Simulation II, the Ca2p/Sr3d intensity ratios remain approximately 3 times larger than those obtained in the experiment. It was not possible to find a nanoparticle input morphology for the SESSA simulations that yields ratios in closer agreement with the experiment, while keeping the correct shape of the in-depth profile.

Nevertheless, the SESSA simulations underpin the previous assumptions that the nanoparticles neither exhibit a homogeneous $Ca_{0.5}Sr_{0.5}F_2$ composition nor a distinct CaF_2–SrF_2 core–shell morphology. Instead, Simulation II indicates that an enrichment of Ca at the surface and an enrichment of Sr inside the nanoparticle is a good approximation of the overall morphology of the real samples. A possible explanation for the remaining deviation between Simulation II and experiment could be an inaccuracy of the used theoretical photoionization cross sections of Ca2p and Sr3d for the specific SR-XPS excitation energies. As shown already in Section 3.3 of this paper, a successful quantification of the Al Kα excitation XPS spectra was only possible by using empirical sensitivity factors determined with qualified reference samples, because the use of standard-free sensitivity factors of Ca2p and Sr3d led to wrong results (for details, see Section 1.2 "Determination of sensitivity factors (SFs) for quantification" in the Supporting Information). Another factor that is expected to cause a deviation between simulation and experiment is the ideality of the selected SESSA input morphologies. All simulations are based on the model of a perfect sphere, neither considering the nonsphericity nor the polydispersity of the real samples (cf. Figure 2). Wang et al. have already shown in detail that significant deviations between SESSA and experimental results can be caused by nonuniformities of core–shell nanoparticles.[28]

4 | DISCUSSION

The formation of nanoparticles during the presented fluorolytic sol–gel synthesis is confirmed by STEM and DLS analyses. These nanoparticles are not spherical and exhibit a quite high polydispersity. The goal of the stepwise synthesis procedure, consisting of two separate fluorinations, was the formation of nanoparticles with a SrF_2–CaF_2 or CaF_2–SrF_2 core–shell morphology, respectively. STEM analysis reveals that no distinct core–shell morphology with a sharp interface between the two fluoride phases is formed. Such a clear separation would cause a corresponding material contrast between core and shell region in the STEM micrographs, which is not observed. At the same time, SR-XPS supported by SESSA simulations confirms an excess of calcium at the surface of the nanoparticles. The combination of STEM and SR-XPS suggests that there is not a clear core–shell morphology but instead an enrichment of calcium at the surface and of strontium in the center of the particles. Consequently, intermixing of calcium and strontium containing phases occurs. This is in accordance with previous results from ^{19}F NMR spectroscopy, also revealing CaF_2-rich domains, SrF_2-rich domains, and an intermixing zone.[13] However, NMR spectroscopy cannot distinguish which domain is the shell and which is the core. The intermixing lowers the difference in material contrast and, thus, makes it more complicated to detect local calcium and strontium enrichments by STEM. Furthermore, SR-XPS is an ensemble method in contrast to STEM. The number of particles included in the analysis is higher by orders of magnitude. Therefore, SR-XPS has a higher probabilty to detect the surface enrichment of one metal, espacially if this enrichment is differently pronounced for different particles in the sample. Quite unexpectedly, both STEM and SR-XPS show no significant difference between the nanoparticles resulting from the Sr–Ca or the Ca–Sr synthesis route. This finding suggests that the chronology of addition and

fluorination of either calcium or strontium lactate does not play a role for the internal morphology of the final nanoparticles.

The quantitative analysis of the nanoparticle suspensions by laboratory-based Al Kα excitation XPS revealed that in Steps (2) and (4) of both nanoparticle synthesis routes, stoichiometric metal fluoride (MF$_2$) nanoparticles are formed. This is indicated by the F/(Ca + Sr) ratio of 2.0, which is obtained both before and after purification of the suspensions by dialysis. However, Step (3) of both synthesis routes exhibits a much lower F/(Ca + Sr) ratio of approximately 1.2 after purification by dialysis. Consequently, at this point, the nanoparticles cannot consist of MF$_2$ alone, but additional metal ions are present, presumably organized in a surface layer. Furthermore, the nanoparticles contain 6 times more carbon and oxygen in Step (3) than in all other steps. This indicates that due to the low amount of fluorine ions available at this point of the synthesis, lactate ions were incorporated as counter ions instead. A higher amount of lactate in the sample Sr–Ca(3) is further confirmed by the slight shift of the Ca2p signal towards lower binding energies compared with the following synthesis step. Apart from the samples Sr–Ca(1) and Ca–Sr(1), which contain the pure metal lactates, the binding energies of all calcium, strontium, and fluorine signals of all other samples confirm the formation of MF$_2$ at all synthesis steps.

At Step (3) of the synthesis, the nanoparticles exhibit an excess of the metal, which was added first. However, laboratory-based Al Kα excitation XPS cannot tell whether this metal is located in the center or at the surface of the particle. This excess vanishes after the second fluorination and the final nanoparticles contain the different metal atoms at almost equal amounts (consistent with the amounts of calcium and strontium added during synthesis). The nanoparticles that are formed during the first fluorination of the Ca–Sr synthesis route contain the entire amount of calcium, which was added. With respect to the SR-XPS results, these particles seem to be unstable. During the second fluorination step, a reconstruction of the entire nanoparticle occurs, resulting in a SrF$_2$-rich domain in the center and a CaF$_2$-rich domain at the surface of the nanoparticles. Regardless of the chronology of synthesis, nearly equal particles are formed. Because there is no sharp interface between calcium and strontium containing phases in the particles but intermixing instead, there must be a significant reconstruction of the initially formed nanoparticles in both synthesis routes.

It should be noted that the applied synthesis procedure as well as the performed laboratory-based XPS experiments is remarkably reproducible. Even though the Sr–Ca(4) and Ca–Sr(4) and their replicates Sr–Ca(4)-II and Ca–Sr(4)-II have been prepared by different synthesists, the XPS spectra are in excellent agreement, both in terms of peak area and binding energy.

5 | CONCLUSIONS

The fluorolytic sol–gel synthesis performed in a stepwise manner was investigated. It comprises a first fluorination of calcium lactate followed by a second fluorination of strontium lactate or vice versa, with the goal to generate nanoparticles with either a SrF$_2$– CaF$_2$ or CaF$_2$–SrF$_2$ core–shell morphology, respectively. The generation of nanoparticles during the synthesis was confirmed by high-resolution STEM and DLS. Laboratory-based Al Kα excitation XPS was applied to monitor the overall chemical composition of the nanoparticle samples at each step of the synthesis. Furthermore, SR-XPS elucidated the change of the samples' chemical composition with depth. The simulation of Ca2p/Sr3d XPS intensity ratio in-depth profiles by SESSA was performed to support the interpretation of the SR-XPS results. STEM investigations allowed for statements about the distribution of calcium and strontium within individual nanoparticles.

It could be shown that there is an enrichment of calcium at the surface and an enrichment of strontium in the core of the nanoparticles, no matter whether the synthesis was started with the fluorination of calcium or strontium lactate. The results suggest that the chronology of the fluorinations does not significantly impact the internal morphology of the final nanoparticles. In principle, core–shell like particle morphologies are formed but without a sharp interface between calcium and strontium containing phases. In other words, there is intermixing between a calcium-enriched surface region and a strontium-enriched core region. Furthermore, the final nanoparticles clearly consist of stoichiometric metal fluoride (MF$_2$) exclusively and contain both metal ions strontium and calcium at equal amounts.

The results of the present paper for undoped nanoparticles are in good agreement with luminescence and NMR results from previous investigations of SrF$_2$–CaF$_2$ core–shell like nanoparticles doped with rare-earth metal ions.[13] However, the XPS study provides additional information that is hardly accessible by luminescence and NMR experiments. This information is crucial, in order to further improve the synthesis of such core–shell like systems in a controlled manner and, thus, ensure a correct interpretation of the luminescence properties of these systems in the future.

ORCID

Anja Müller 🅭 https://orcid.org/0000-0003-2085-3687
Jörg Radnik 🅭 https://orcid.org/0000-0003-0302-6815
Wolfgang E.S. Unger 🅭 https://orcid.org/0000-0002-7670-4042

REFERENCES

1. Haase M, Schäfer H. Upconverting nanoparticles. *Angew Chem Int Ed*. 2011;50(26):5808-5829.

2. Gai S, Li C, Yang P, Lin J. Recent progress in rare earth micro/nanocrystals: soft chemical synthesis, luminescent properties, and biomedical applications. *Chem Rev*. 2014;114(4):2343-2389.

3. Zhou J, Liu Q, Feng W, Sun Y, Li F. Upconversion luminescent materials: advances and applications. *Chem Rev*. 2015;115(1):395-465.

4. Wang G, Peng Q, Li Y. Upconversion luminescence of monodisperse $CaF_2:Yb^{3+}/Er^{3+}$ nanocrystals. *J am Chem Soc*. 2009;131(40):14200-14201.

5. Song L, Gao J, Song R. Synthesis and luminescent properties of oleic acid (OA)-modified CaF_2: Eu nanocrystals. *JOL*. 2010;130(7):1179-1182.

6. Dong N-N, Pedroni M, Piccinelli F, et al. NIR-to-NIR two-photon excited $CaF_2:Tm^{3+},Yb^{3+}$ nanoparticles: multifunctional nanoprobes for highly penetrating fluorescence bio-imaging. *ACS Nano*. 2011;5(11):8665-8671.

7. Song L, Gao J, Li J. Sensitized luminescence of water-dispersible CaF_2: RE^{3+} (RE=Eu, Tb, Ce/Tb) nanoparticles through surfactant coating ligands. *JOL*. 2014;151:18-21.

8. Ritter B, Haida P, Fink F, et al. Novel and easy access to highly luminescent Eu and Tb doped ultra-small CaF_2, SrF_2 and BaF_2 nanoparticles—structure and luminescence. *Dalton Trans*. 2017;46(9):2925-2936.

9. Du Y-P, Sun X, Zhang Y-W, Yan Z-G, Sun L-D, Yan C-H. Uniform alkaline earth fluoride Nanocrystals with diverse shapes grown from thermolysis of metal trifluoroacetates in hot surfactant solutions. *Cryst Growth des*. 2009;9(4):2013-2019.

10. Kim SY, Woo K, Lim K, Lee K, Jang HS. Highly bright multicolor tunable ultrasmall beta-Na(Y,Gd)F(4):Ce,Tb,Eu/beta-NaYF(4) core/shell nanocrystals. *Nanoscale*. 2013;5(19):9255-9263.

11. Huang X. Realizing efficient upconversion and down-shifting dual-mode luminescence in lanthanide-doped $NaGdF_4$ core–shell–shell nanoparticles through gadolinium sublattice-mediated energy migration. *Dyes Pigm*. 2016;130:99-105.

12. Zhou B, Tao L, Chai Y, Lau SP, Zhang Q, Tsang YH. Constructing interfacial energy transfer for photon up- and down-conversion from lanthanides in a core-shell nanostructure. *Angew Chem Int Ed*. 2016;55(40):12356-12360.

13. Ritter B, Haida P, Krahl T, Scholz G, Kemnitz E. Core–shell metal fluoride nanoparticles via fluorolytic sol–gel synthesis—a fast and efficient construction kit. *J Mater Chem C*. 2017;5(22):5444-5450.

14. Kemnitz E, Groß U, Rüdiger S, Shekar CS. Amorphous metal fluorides with extraordinary high surface areas. *Angew Chem Int Ed*. 2003;42(35):4251-4254.

15. Rüdiger S, Kemnitz E. The fluorolytic sol-gel route to metal fluorides—a versatile process opening a variety of application fields. *Dalton Trans*. 2008;(9):1117-1127.

16. Kemnitz E, Noack J. The non-aqueous fluorolytic sol–gel synthesis of nanoscaled metal fluorides. *Dalton Trans*. 2015;44(45):19411-19431.

17. Ritter B, Krahl T, Rurack K, Kemnitz E. Nanoscale CaF_2 doped with Eu^{3+} and Tb^{3+} through fluorolytic sol–gel synthesis. *J Mater Chem C*. 2014;2(40):8607-8613.

18. Rivière JC, Myhra S. *Handbook of Surface and Interface Analysis: Methods for Problem-Solving*. Second ed. Boca Raton: CRC Press; 2009.

19. Weigert F, Müller A, Hausler I, et al. Combining HR-TEM and XPS to elucidate the core-shell structure of ultrabright CdSe/CdS semiconductor quantum dots. *Sci Rep*. 2020;10(1):20712.

20. Müller A, Sparnacci K, Unger WES, Tougaard S. Determining nonuniformities of core-shell nanoparticle coatings by analysis of the inelastic background of X-ray photoelectron spectroscopy survey spectra. *Surf Interface Anal*. 2020;52(11):770-777.

21. Cant DJH, Minelli C, Sparnacci K, et al. Surface-energy control and characterization of nanoparticle coatings. *J Phys Chem C*. 2020;124(20):11200-11211.

22. Shard AG. X-Ray photoelectron spectroscopy. In: *Characterization of Nanoparticles*. Amsterdam: Elsevier; 2020:349-371.

23. Müller A, Heinrich T, Tougaard S, et al. Determining the thickness and completeness of the shell of polymer core-shell nanoparticles by X-ray photoelectron spectroscopy, secondary ion mass spectrometry, and transmission scanning electron microscopy. *J Phys Chem C*. 2019;123(49):29765-29775.

24. Baer DR, Artyushkova K, Brundle CR, et al. Practical guides for X-ray photoelectron spectroscopy (XPS): first steps in planning, conducting and reporting XPS measurements. *J Vac Sci Technol a*. 2019;37.

25. Cant DJ, Clifford CA, Shard AG, Müller A, Unger WES. Towards standardising electron spectroscopy measurement of nanoparticle coatings. *J Surf Anal*. 2019;26(2):164-165.

26. Powell CJ, Werner WSM, Kalbe H, Shard AG, Castner DG. Comparisons of analytical approaches for determining shell thicknesses of core–shell nanoparticles by X-ray photoelectron spectroscopy. *J Phys Chem C*. 2018;122(7):4073-4082.

27. Belsey NA, Cant DJH, Minelli C, et al. Versailles project on advanced materials and standards interlaboratory study on measuring the thickness and chemistry of nanoparticle coatings using XPS and LEIS. *J Phys Chem C*. 2016;120:24070-24079.

28. Wang Y-C, Engelhard MH, Baer DR, Castner DG. Quantifying the impact of nanoparticle coatings and nonuniformities on XPS analysis: gold/silver core–shell nanoparticles. *Anal Chem*. 2016;88(7):3917-3925.

29. Tao F, Grass ME, Zhang Y, et al. Reaction-driven restructuring of Rh-Pd and Pt-Pd core-shell nanoparticles. *Science*. 2008;322(5903):932-934.

30. Abel KA, Boyer J-C, van Veggel FCJM. Hard proof of the NaYF4/NaGdF4 nanocrystal core/shell structure. *J am Chem Soc*. 2009;131(41):14644-14645.

31. Doh WH, Papaefthimiou V, Dintzer T, Dupuis V, Zafeiratos S. Synchrotron radiation X-ray photoelectron spectroscopy as a tool to resolve the dimensions of spherical core/shell nanoparticles. *J Phys Chem C*. 2014;118(46):26621-26628.

32. Borchert H, Haubold S, Haase M, et al. Investigation of ZnS Passivated InP Nanocrystals by XPS. *Nano Lett*. 2002;2(2):151-154.

33. ISO 18115-1:2013, Surface Chemical Analysis—Vocabulary—Part 1: General Terms and Terms Used in Spectroscopy (https://www.iso.org/standard/63783.html).

34. Girard-Lauriault PL, Gross T, Lippitz A, Unger WES. Chemical and elemental depth profiling of very thin organic layers by constant kinetic energy XPS: a new synchrotron XPS analysis strategy. *Anal Chem*. 2012;84(14):5984-5991.

35. Smekal W, Werner WSM, Powell CJ. Simulation of electron spectra for surface analysis (SESSA): a novel software tool for quantitative auger-electron spectroscopy and X-ray photoelectron spectroscopy. *Surf Interface Anal*. 2005;37(11):1059-1067.

36. Krahl T, Broßke D, Scheurell K, Lintner B, Kemnitz E. Novel aspects in the chemistry of the non-aqueous fluorolytic sol–gel synthesis of nanoscaled homodisperse MgF_2 sols for antireflective coatings. *J Mater Chem C*. 2016;4(7):1454-1466.

37. ISO 15472:2010, Surface Chemical Analysis—X-Ray Photoelectron Spectrometers—Calibration of Energy Scales (https://www.iso.org/standard/55796.html).

38. Hesse R. Universal spectrum processing, analysis, and presentation software for photoelectron spectra (XPS). *X-Ray Absorption Spectra (XAS) and RAMAN Spectra UNIFIT*. Version 2020

39. Tanuma S, Powell CJ, Penn DR. Calculations of electron inelastic mean free paths. *Surf Interface Anal*. 1994;21(3):165-176.

40. Kragten J. Calculating standard deviations and confidence intervals with a universally applicable spreadsheet technique. *Analyst*. 1994; 119(10):2161-2165.

41. Seah MP. Summary of ISO/TC 201 standard: VII ISO 15472: 2001—surface chemical analysis—X-ray photoelectron spectrometers—calibration of energy scales. *Surf Interface Anal*. 2001; 31(8):721-723.

42. Vasquez RP. X-ray photoelectron spectroscopy study of Sr and Ba compounds. *J Electron Spectrosc Relat Phenom*. 1991;56(3): 217-240.

43. Briggs D, Seah MP. *Practical Surface Analysis by Auger and X-Ray Photoelectron Spectroscopy*. Hoboken: John Wiley & Sons; 1990.

44. Cooper JW. Photoelectron-angular-distribution parameters for rare-gas subshells. *Phys Rev a*. 1993;47(3):1841-1851.

45. Trzhaskovskaya MB, Nefedov VI, Yarzhemsky VG. Photoelectron angular distribution parameters for elements Z=1 to Z=54 in the photoelectron energy range 100-5000 eV. *At Data Nucl Data Tables*. 2001;77(1):97-159.

SUPPORTING INFORMATION

Additional supporting information may be found online in the Supporting Information section at the end of this article.